J Mater Sci (2020) 55:15826–15844

Computation & theory

Adsorption mechanism of toxic heavy metal ions on oxygen-passivated nanopores in graphene nanoflakes

Hamid Reza Ghenaatian[1,*], Mehdi Shakourian-Fard[2,*], and Ganesh Kamath[3]

[1] Department of Physics, Jahrom University, P.O. Box 74135-111, Jahrom, Iran
[2] Department of Chemical Engineering, Birjand University of Technology, P.O. Box 97175/569, Birjand, Iran
[3] Dalzierfiver LLC, 3500 Carlfied St, El Sobrante, CA 94803, USA

Received: 4 June 2020
Accepted: 11 August 2020
Published online: 31 August 2020

ABSTRACT

In this work, using density functional theory, we investigate the adsorption process of toxic metal ions (Hg^{2+}, Cd^{2+}, and Pb^{2+}) on graphene nanoflakes (GNF) comprised of various sized oxygen-passivated nanopores to gain molecular insights into the ability of such surfaces in effectively removing the metal ions from contaminated environments. Thermodynamically, the adsorption of these ions on the oxygen-passivated nanopores is shown to be more energetically favorable than that on the pristine surface. The dispersion corrected adsorption energy calculations indicate Hg^{2+} ion to have the highest and Pb^{2+} ion the lowest affinities for interaction with such surfaces ($Hg^{2+} > Cd^{2+} > Pb^{2+}$). The highest adsorption of Hg^{2+} and Cd^{2+} ions on the surfaces is seen in the 12-crown-3…Hg^{2+} (− 382.9 kcal/mol) and 12-crown-3…Cd^{2+} (− 314.7 kcal/mol) complexes, while Pb^{2+} ion shows the highest adsorption energy for the 18-crown-6 surface (− 195.0 kcal/mol). Noncovalent interaction plots, Hirshfeld charge analysis and energy decomposition analysis conclude that the role of charge transfer in formation of surface…ion complexes is more important than noncovalent interactions and therefore plays a key role in the adsorption of these ions on the surfaces. The magnitude of charge transfer in the complexes follows the order: surface…Hg^{2+} > surface…Cd^{2+} > surface…Pb^{2+}, which is consistent with the adsorption energetic order of these metal ions on the surfaces. We also found that Pb^{2+} ion is mainly adsorbed on the surfaces via electrostatic interactions, while Hg^{2+} and Cd^{2+} ions are adsorbed through van der Waals (vdW) interactions. This could be attributed to the presence of vacant p orbitals on Pb^{2+} ion, which interact with the π bonds on the GNF and oxygen

Handling Editor: Christopher Blanford.

Address correspondence to E-mail: Ghenaat@jahromu.ac.ir; shakourian@birjandut.ac.ir

https://doi.org/10.1007/s10853-020-05113-4

atoms in the nanopores through electrostatic interactions. No such vacant orbitals are available for Hg^{2+} and Cd^{2+} ions thus resulting in such ions adsorbing via vdW interactions. The contribution of ΔE_{orb}, induction energy component of total energy, for the surface…Hg^{2+} complexes is more than that for the surface…Cd^{2+} and surface…Pb^{2+} complexes, following the order: surface…Hg^{2+} > surface…Cd^{2+} > surface…Pb^{2+} again, consistent with the calculated adsorption energy order suggesting that charge transfer indeed plays a major role in formation of such surface…ion complexes. Finally, time-dependent density functional theory calculations show that the absorption spectra of the surfaces undergo significant changes, including peak shifts, peak quenching and appearance of new peaks, upon interaction with Hg^{2+}, Cd^{2+}, and Pb^{2+} ions, such changes being consistent with binding energetics rank order of ions on these surfaces. These complexes would have potential applications in near-infrared photonics in addition to their service of effectively remediating of toxic heavy elements from contaminated environments.

GRAPHIC ABSTRACT

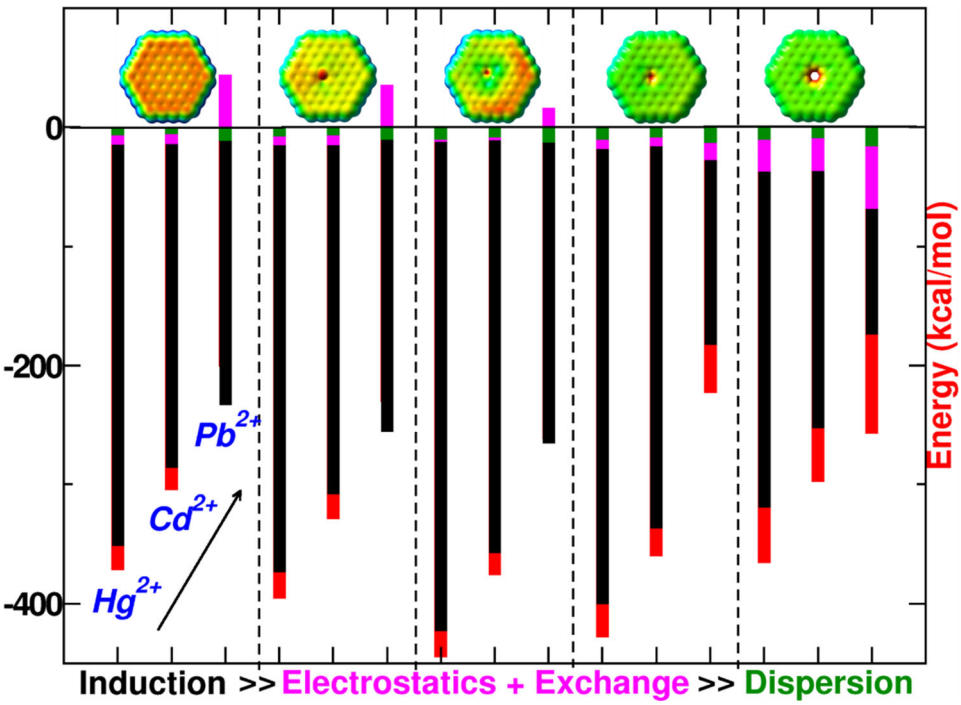

Introduction

Among all the pollutants, heavy metal toxicity is a serious threat and has resulted in several health disorders and diseases. Toxic heavy metals (THMs) as an environmental contaminant can emanate from both natural and anthropogenic processes and are not metabolized by the body while found to accumulate in the soft tissues. Therefore, in recent years, the global demand for removal of THMs from drinking water, sewage, aquatic flora and fauna and

wastewaters is of vital importance from health and economic points of view [1, 2]. In order to protect humanity from the most dangerous toxic heavy metals, the World Health Organization (WHO) has implemented environmental regulations for international health matters and public health [3]. According to the WHO requirements, the three most THMs, namely cadmium (Cd), mercury (Hg), and lead (Pb), should be separated from drinking water, wastewaters, food products and biological fluids because of their extreme environmental, public health and economic impacts.

Graphene, as a two-dimensional material composed of sp^2-conjugated carbon atoms, can be potentially considered as an ideal nano-membrane [4]. Pristine defect-free monolayer graphene is impermeable to both gaseous and liquid molecules. Nowadays, extensive research efforts have been focused on development of graphene-family materials, including epitaxial graphene, graphene quantum dots, reduced graphene oxide (rGO), graphene oxide (GO), hybrid of GO or rGO to name a few with a myriad of materials such as magnetic nanoparticles, organic, inorganic, and polymeric materials, etc., thereby using these fabricated nanocomposites as possible candidates for detection and separation of toxic heavy metals [5–10]. Recently, the performance of graphene-based materials for removing various water pollutants such as anions, metallic ions, salts, and organic chemicals from aqueous media has been evaluated using molecular dynamics simulations [11]. GO has displayed good performance as adsorbent for efficient elimination of heavy metal ions from wastewater because of the large number of functional surface groups and high surface area. Guerrero-Fajardo et al. [12] synthesized GO as adsorbent and considered its performance for removal of various heavy metal ions from aqueous solution. They found that the high adsorption capacity of metal ions on the GO surface is due to its hydrophilic properties and the presence of functional groups containing oxygen atoms.

Kong et al. [13] also synthesized GO surface and experimentally determined the adsorption capacity of metallic hard, soft and transition metal ions on the oxygen modified surface. They found that the adsorption capacity of hard ions is substantially lower than that of soft and borderline ones. These experimental studies were complemented by DFT calculations. El-Fawal et al. [14] synthesized the hybrid of GO with Fe_3O_4 nanoparticles (Fe_3O_4/GO) and used it for removal of hydrated heavy metal ions from water. They further investigated the removal mechanism of toxic heavy metal ions onto the prepared Fe_3O_4/GO using DFT calculations. Graphene and GO-based composite materials are excellent candidates for water treatment and desalination due to their high porosity, large specific surface area, excellent electrical conductivity, mechanical properties, and thermal stability [15]. Li et al. [16] have studied the application of GO/chitosan composite for wastewater adsorption treatment. They indicated that GO/chitosan composite has a larger adsorption capacity than GO and chitosan components in removal of heavy metal ions from wastewater samples.

Nanopore technology has emerged as a powerful tool for single-ion channels, single-molecule detection, and liquid purification [17]. Recently, some of studies have shown that defects and micropores may be decorated within the graphene surfaces to improve adsorption [18, 19]. Furthermore, high flow rate water purification filters have been made by creating functionalized nanopores within the graphene membranes [20, 21]. These pores lead to separation of salt ions from water [22]. A wide variety of methods, including electron-beam irradiation, helium-ion beam drilling, ultraviolet-induced oxidative etching, chemical etching, and diblock copolymer templating, has been achieved for creating nanopores in graphene [23–26]. The presence of these nanopores in samples of graphene has been observed through scanning transmission electron microscopy (STEM) measurements [20, 21].

However, the small holes in graphene are reconstructed or undergo the self-healing process (partial or total filling by diffusing carbon or other adatoms). On the other hand, the stabilization of holes, vacancies and defects in graphene can be achieved through passivating agents [27, 28].

Passivation with chosen chemical element leads to charge polarization at the nanopore interface due to electronegativity difference between the passivating entity and carbon, thus forming a trap for positive and negative ions. For example, oxygen passivation leads to negative perimeters at the nanopores. Cation species are attracted to these perimeters, while halogens are driven away from the perimeters [29, 30]. Recently, Guo et al. [29] have synthesized the oxygen-passivated nanopores in graphene surface and

presented their atomic-resolution images. Their results indicated that these nanopores in graphene could selectively bind to various atoms depending on the nanopore size. Heath et al. [31] investigated the interactions between various alkali metal elements (Li, Na, K, Rb, and Cs) and oxygen-passivated nanopores in graphene with application in the development of novel alkali metal battery technologies. Their results indicate that oxygen-passivated nanopores give the strongest binding energy when the size of the nanopore is similar to the element's van der Waals radius. Olsson et al. [32] also investigated the adsorption and migration of Li, Na, and K atoms on the pristine graphene surface and defective graphene surfaces substituted by oxygen and nitrogen atoms to gain insight into the metal storage and mobility in carbon-based anodes for alkali metal batteries. In addition, removal of NaCl salt from water by fluorine-terminated graphene nanopores [33], hydroxyl-terminated graphene nanopores [34] and fluorine-nitrogen-terminated graphene nanopores [35] has been studied through molecular dynamics (MD) simulations in the literature.

To the best of our knowledge, this is the first theoretical study comprehensively investigating the interaction between toxic heavy metal ions (Hg^{2+}, Cd^{2+}, and Pb^{2+}) and oxygen-passivated nanopores in graphene nanoflakes using density functional theory (DFT) calculations. In this study, we aim to understand the adsorption mechanism of Hg^{2+}, Cd^{2+}, and Pb^{2+} metal ions on the surfaces and the effect of the size of oxygen passivated nanopores on the adsorption strength of these ions. Furthermore, the structural, electronic, and optical properties of oxygen-passivated nanopores in graphene nanoflakes are considered with adsorption of these toxic heavy metal ions.

Theory and computational details

Geometries of the pristine graphene nanoflake (GNF) model, GNFs containing oxygen-passivated nanopores and their complexes with three environmentally important heavy metal ions including Hg^{2+}, Cd^{2+}, and Pb^{2+} are fully optimized using the density functional theory (DFT) with CAM-B3LYP functional. CAM-B3LYP is a hybrid exchange–correlation functional [36], which combines B3LYP at short-range with an increasing amount of exact HF exchange at long-range. The Def2-TZVPP basis set was applied for metal ions and 6–31g(*d*,*p*) basis set was used for the C, H, and O atoms in the models. All the geometry optimizations were done using the Gaussian 09 suite of programs [37].

In order to build the GNFs composed of different sizes of oxygen-passivated nanopores, first, the pristine GNF model with 96 carbon atoms and 24 hydrogen atoms (Circumcircumcoronene) was built. Then, four GNFs composed of different sizes of oxygen-passivated nanopores were obtained by removing carbon atoms from the pristine GNF surface and saturating the carbon atoms with oxygen atoms (Fig. 1). The resulting oxygen-passivated nanopores in GNF surface are named crown ether. Therefore, each GNF nanopore is denoted N-crown-M, where N and M represent the number of C and O atoms in the nanopores, respectively. These four structures are identified as 10-crown-2, 12-crown-3, 14-crown-4, and 18-crown-6. The spin multiplicity of the circumcircumcoronene and crown ether surfaces is singlet. Geometry optimization shows that the circumcircumcoronene, 12-crown-3, 14-crown-4, and 18-crown-6 surfaces remain planar upon relaxation, whereas the 10-crown-2 surface is nonplanar. In this surface, oxygen atoms move out of the plane due to small size of the nanopore and repulsion between the lone pairs on the oxygen atoms. Further, it should be pointed out that the diameter of the nanopores containing oxygen atoms follows the order 10-crown-2 > 12-crown-3 > 14-crown-4 > 18-crown-6 [29]. Therefore, it can be interesting to find out the adsorption behavior of Hg^{2+}, Cd^{2+}, and Pb^{2+} ions on the surfaces.

The adsorption energy (ΔE_{ads}) of Hg^{2+}, Cd^{2+}, and Pb^{2+} metal ions on the surfaces is calculated using Eq. 1 as follows:

$$\Delta E_{ads} = E_{ion+substrate} - (E_{substrate} + E_{ion}) + BSSE \quad (1)$$

where $E_{ion\ +\ substrate}$ is the total energy of the ion/substrate system, $E_{substrate}$ is the total energy of the GNF surface or GNFs containing oxygen-passivated nanopores, and E_{ion} is the total energy of an individual metal ion. The calculated adsorption energies are corrected by the basis set superposition errors (BSSEs) calculated with counterpoise method [38]. The ΔE_{ads} is the energy released to form a stable ion/substrate system. A more negative ΔE_{ads} value corresponds to a more stable ion/substrate system. In addition, Grimme's empirical dispersion

correction (D3) was used along with the CAM-B3LYP functional to accurately account for dispersion corrections in the calculated adsorption energies [39].

The thermochemistry properties for adsorption of metal ions on the surfaces, including the enthalpy of adsorption (ΔH_{ads}) and free energy of adsorption (ΔG_{ads}), are calculated at 298.15 K through the difference between the enthalpy/free energy of ion/substrate systems and isolated substrates and metal ions. The HOMO–LUMO energy gap (E_g) values of the surface…ion complexes are calculated based on the energy difference of the lowest unoccupied molecular orbital (LUMO) and the highest occupied molecular orbital (HOMO) of the surface…ion complexes. The charge transfer value between the surfaces and metal ions was calculated through Hirshfeld charge analysis [40]. In order to characterize the nature of interaction between the ions and surfaces, energy decomposition analysis (EDA) was performed and noncovalent interactions were plotted using Multiwfn-3.7 program [41]. The gradient iso-surfaces were plotted using VMD1.9.2 software [42] with an iso-surface of 0.5 a.u. In order to understand the effect of ion adsorption on the absorption spectrum of the surfaces, time-dependent density functional theory (TD-DFT) calculations [43] were carried out on the surfaces before and after complexation with Hg^{2+}, Cd^{2+}, and Pb^{2+} metal ions using the same level of DFT theory (CAM-B3LYP/6–31g(*d*,*p*)/Def2-TZVPP).

Results and discussion

Hg^{2+}, Cd^{2+}, and Pb^{2+} ions adsorption on the surfaces

The electrostatic potential (ESP) iso-surfaces are usually used to predict the local reactivity of the molecules. A site with more negative electrostatic potential in a molecule will more likely attract a site with more positive electrostatic potential [44]. In the ESP iso-surfaces, the points with negative and positive electrostatic potentials are usually observed with red and blue colors, respectively. Therefore, in order to gain insights into the adsorption mechanism of Hg^{2+}, Cd^{2+}, and Pb^{2+} ions on the surfaces, the ESP iso-surfaces of the surfaces at an isovalue electron density of 0.0004 a.u. are calculated and are shown in Fig. 2. The ESP iso-surfaces of the Hg^{2+}, Cd^{2+}, and Pb^{2+} ions are not shown in Fig. 2 because they are positive species and have completely blue color. It can be noticed from Fig. 2 that the aromatic rings in the circumcircumcoronene surface show a uniform negative electrostatic potential (the red color). Therefore, these are potentially good sites for interaction with the positive Hg^{2+}, Cd^{2+}, and Pb^{2+} ions.

The creation of oxygen-passivated nanopores in the circumcircumcoronene nanoflake changes the ESP iso-surface. As seen from Fig. 2, the ESP iso-surfaces of the 10-crown-2 and 12-crown-3 surfaces exhibit some local inhomogeneities in the carbon atoms of the surfaces, while those of 14-crown-4 and 18-crown-6 show homogenous distribution of the electrostatic potential in the carbon atoms. However, the oxygen atoms at the nanopores have the highest negative electrostatic potential (the red color) in all the surfaces due to higher electronegativity of oxygen atoms than carbon atoms. Therefore, the presence of negative electrostatic potential around the oxygen atoms in the nanopores provides more reactive areas than other regions on the surfaces and thereby enhances the interaction strength between the surfaces and Hg^{2+}, Cd^{2+}, and Pb^{2+} ions.

In order to find the most stable geometry of ions on the pristine graphene model, three sites are normally considered, namely, the T site (the top of a carbon atom), the H site (a hollow site on top of aromatic hexagonal ring), and the B site (a bridge site at the midpoint of the C–C bond) [32, 45–48]. The Hg^{2+}, Cd^{2+}, and Pb^{2+} ions are placed at the vertical distance of 2.7 Å from these sites. In addition, these ions are placed at the distance of 2.7 Å from the center of the nanopores and close to the oxygen atoms. These structures are optimized at the CAM-B3LYP/6–31g(*d*,*p*)/Def2-TZVPP level of theory and the most stable geometries are shown in Figs. 3 and 4. It should be mentioned that the final coordinates for Hg^{2+}, Cd^{2+}, and Pb^{2+} ions on the surfaces are almost identical to the initial configuration even upon geometry optimization.

The thermochemistry parameters and electronic properties of these surface ion (ion = Hg^{2+}, Cd^{2+} and Pb^{2+}) complexes are also calculated and are summarized in Tables 1 and 2, respectively.

From Fig. 3, it is clear that the most energetically-favorable binding site for adsorption of metal ions on the circumcircumcoronene surface is the hollow site on top of aromatic hexagonal rings. The nearest equilibrium distances of Hg^{2+}, Cd^{2+}, and Pb^{2+} ions

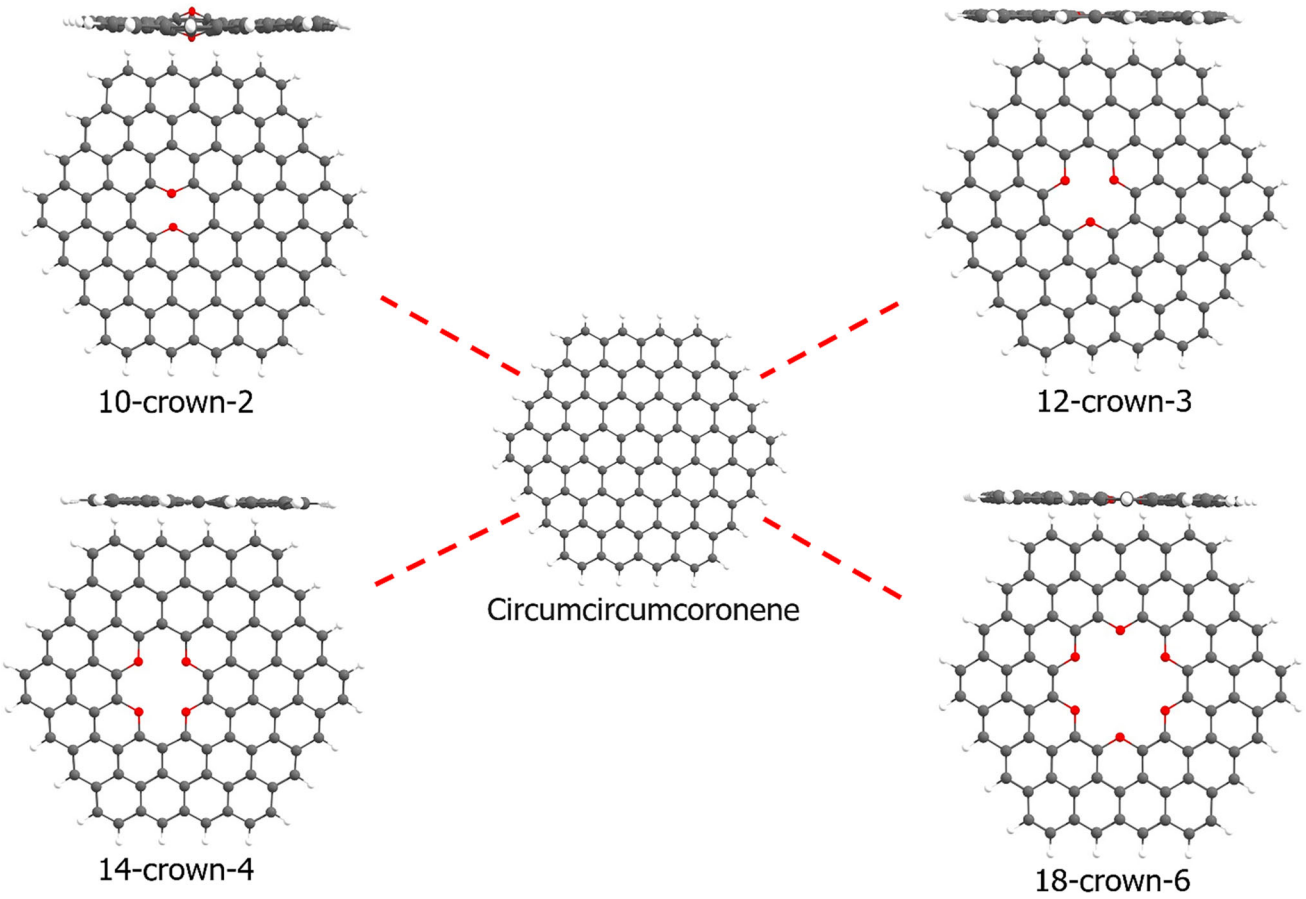

Figure 1 The optimized structures of circumcircumcoronene and graphene nanoflakes containing oxygen-passivated nanopores.

from the circumcircumcoronene surface are 4.054 Å, 4.186 Å, and 2.256 Å, respectively (see Table 2). In addition, the ion adsorption on the circumcircumcoronene surface does not cause curvature in the circumcircumcoronene surface. Results reported in the literature show that Hg^{2+}, Cd^{2+}, and Pb^{2+} ions are preferentially adsorbed on a smaller model than circumcircumcoronene, which is named circumcoronene ($C_{54}H_{18}$), at the T, B, and H sites, respectively [46]. A comparison between this result [46] and our results for adsorption of these ions on the circumcircumcoronene surface reveals that the size of pristine graphene model affects the binding position of these ions. With increasing the size of graphene model from circumcoronene to circumcircumcoronene model, the tendency of these ions increases for adsorption at the hollow site on top of aromatic hexagonal rings.

As seen from Fig. 3, the Hg^{2+}, Cd^{2+}, and Pb^{2+} ions in the 10-crown-2…ion (ion = Hg^{2+}, Cd^{2+} and Pb^{2+}) complexes stay above the six-membered rings containing oxygen at the distances of 3.933, 4.00, and 2.560 Å from the nearest oxygen atom, respectively. Upon adsorption of the ions on the 12-crown-3, 14-crown-4, and 18-crown-6 surfaces, the oxygen-passivated nanopores remain flat, except for adsorption of Hg^{2+} and Cd^{2+} ions on the 18-crown-6 surface (Figs. 3, 4). On the other hand, in all the surface…ion complexes, the ions prefer to stay above the surfaces with the exception of 18-crown-6…Pb^{2+} complex. In this 18-crown-6…Pb^{2+} complex, the Pb^{2+} ion moves from the top of 18-crown-6 surface into the nanopore. It seems that the size of nanopore in the 18-crown-6 surface is conducive for trapping of the Pb^{2+} ion by the oxygen atoms. A comparison of the nearest distance between the ions and the oxygen atoms in the nanopores shows that the distances follow the order $Cd^{2+} > Hg^{2+} > Pb^{2+}$ in all the surface…ion complexes.

To quantify the adsorption process of ions on the surfaces, the enthalpy of adsorption (ΔH_{ads}) and free energy of adsorption (ΔG_{ads}) of Hg^{2+}, Cd^{2+}, and Pb^{2+}

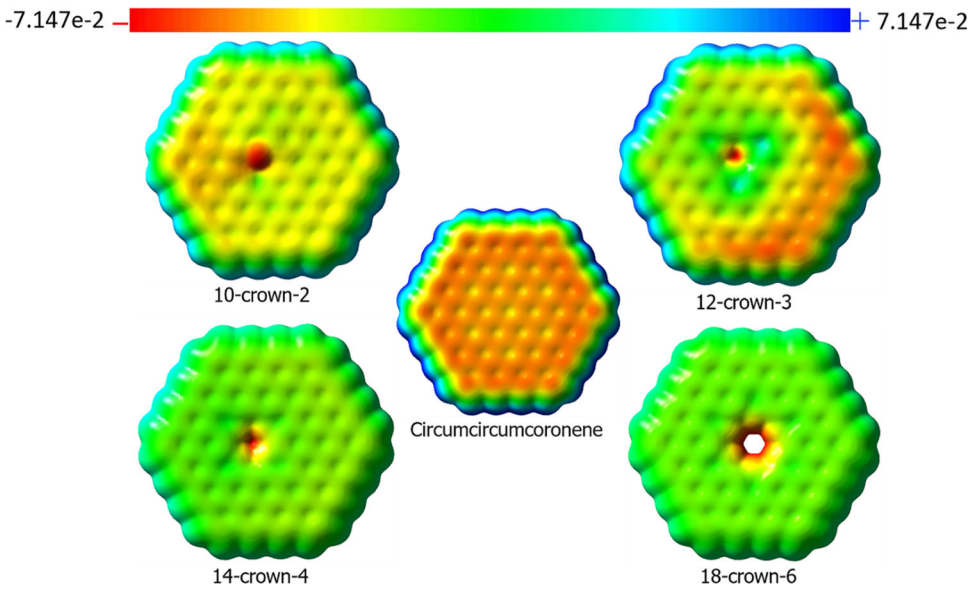

Figure 2 Electrostatic potential (ESP) iso-surfaces of the circumcircumcoronene and GNFs containing oxygen-passivated nanopores at an isovalue electron density of 0.0004 a.u., calculated at the CAM-B3LYP/6–31g(*d*,*p*)/Def2-TZVPP level of theory (blue/yellow to red color scale represents the positive and negative electrostatic potentials, respectively).

ions on the surfaces are calculated. The negative values of ΔH_{ads} and ΔG_{ads} suggest that the surface…ion complex formation is an exothermic and favorable reaction and proceeds spontaneously. Table 1 shows that the formation of surface…Hg^{2+} complexes are more favorable than that of surface…Cd^{2+} and surface…Pb^{2+} complexes. The order of ΔH_{ads} and ΔG_{ads} values for the surface…ion complexes is as follows surface…Hg^{2+} > surface…Cd^{2+} > surface…Pb^{2+}.

The adsorption energy of ions on the surfaces is closely related to the stability and binding ability of the corresponding surface…ion complex. The adsorption energy of a stable complex is usually negative, and a more negative value for adsorption energy means a stronger adsorption ability. Therefore, the coupling strength between the Hg^{2+}, Cd^{2+}, and Pb^{2+} ions and the surfaces is considered by calculating their respective adsorption energies (ΔE_{ads}) using Eq. 1. The negative values of adsorption energies (ΔE_{ads}) summarized in Table 1 indicate that the adsorption of Hg^{2+}, Cd^{2+}, and Pb^{2+} ions on the surfaces is energetically favorable. In order to accurately account for dispersion effects in DFT, D3 dispersion correction was added to the calculated ΔE_{ads} values. Our results show that the ΔE_{ads} values for adsorption of ions on the circumcircumcoronene and nanopore surfaces change by about 3–15 kcal/mol.

From comparison of the ΔE_{ads} + D3 values of ions on the circumcircumcoronene surface, it can be seen that the adsorption strength of Hg^{2+} ion on the circumcircumcoronene surface is more than Cd^{2+} and Pb^{2+} ions and follows the order circumcircumcoronene…Hg^{2+} (− 314.6 kcal/mol) > circumcircumcoronene…Cd^{2+} (− 248.1 kcal/mol) > circumcircumcoronene…Pb^{2+} (− 141.2 kcal/mol). This order is in accordance with previous study for adsorption of these metal ions on the circumcoronene model [46]. From the ΔE_{ads} + D3 values summarized in Table 1, it can be clearly seen that the presence of oxygen-passivated nanopores in GNF surface has a marked impact on the adsorption energy of ions. The ΔE_{ads} + D3 values of these ions on the oxygen-passivated nanopores are found to follow the order Hg^{2+} > Cd^{2+} > Pb^{2+}. This order is similar to the observed trend for ΔH_{ads} and ΔG_{ads} values of surface…ion complexes.

The changes in adsorption energy, enthalpy of adsorption and free energy of adsorption of the surface…ion complexes are shown in Fig. 5. As seen from Fig. 5, the ΔE_{ads} + D3, ΔH_{ads} and ΔG_{ads} values for adsorption of Hg^{2+} and Cd^{2+} ions on the surfaces follows the order 12-crown-3 > 14-crown-4 > 10-crown-2 > circumcircumcoronene > 18-crown-6.
This order for adsorption of Pb^{2+} ion changes to 18-crown-6 > 12-crown-3 > 14-crown-4 > 10-crown-2 > circumcircumcoronene. It seems that there are two contributing factors whose subtle balance affects the adsorption strength of each ion on the oxygen-passivated nanopores, viz. the number of oxygen atoms in the nanopores and the size of nanopores. As both oxygen atoms on the 10-crown-2 surface are not on one side of the surface, these ions can interact with

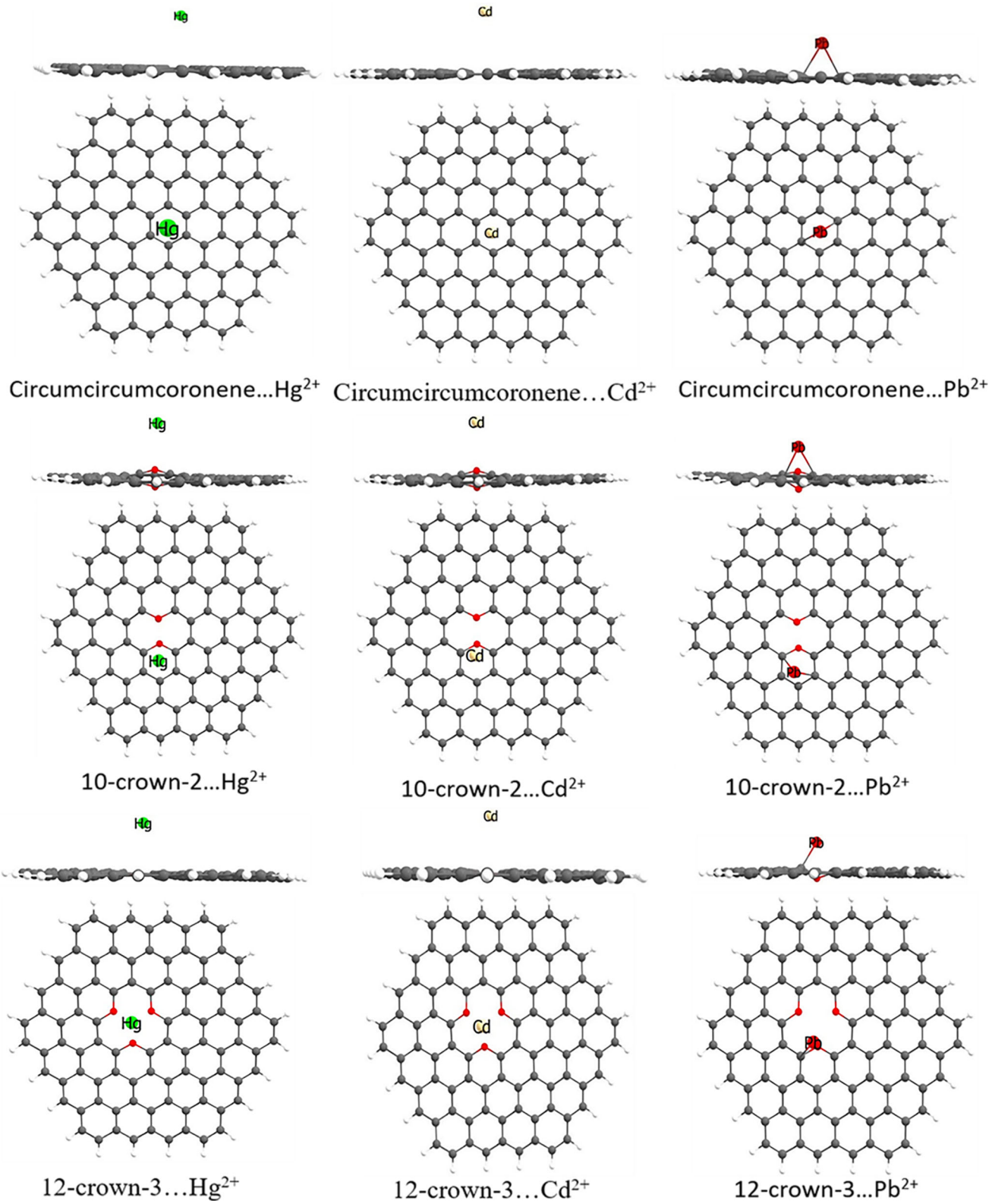

Figure 3 Top and side view of the optimized structures of circumcircumcoronene, 10-crown-2 and 12-crown-3 surfaces after complexation with Hg^{2+}, Cd^{2+}, and Pb^{2+} ions.

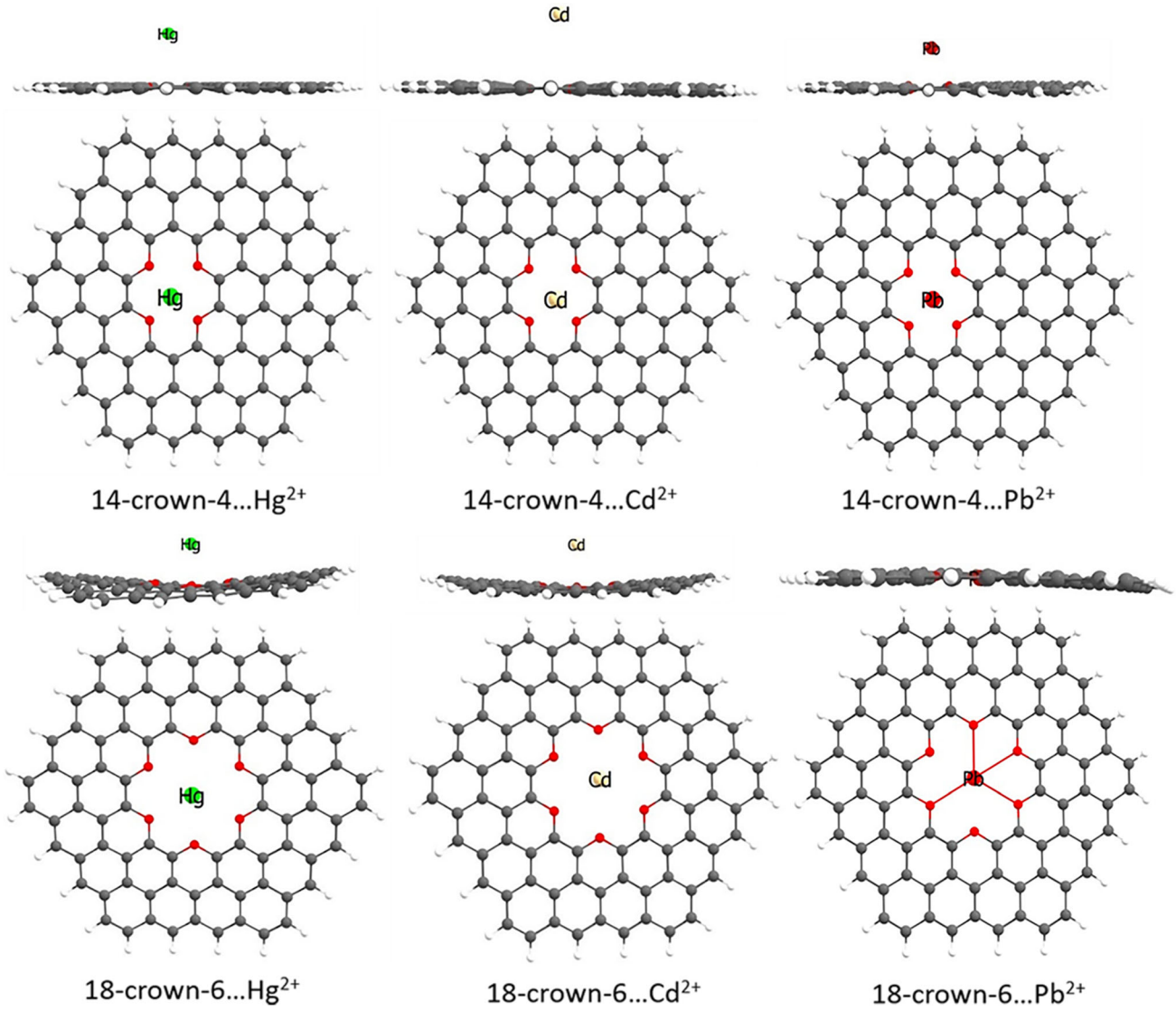

Figure 4 Top and side view of the optimized structures of 14-crown-4 and 18-crown-6 surfaces after complexation with Hg^{2+}, Cd^{2+}, and Pb^{2+} ions.

only one of the oxygen atoms. With increasing number of oxygen atoms from 2 in the 10-crown-2 surface to 3 on the 12-crown-3 surface, the ΔE_{ads} + D3 value for the surface…ion complexes increases (lower negative values). This is due to interaction of three oxygen atoms with the ions. When going from 12-crown-3 to 14-crown-4 surface, the ΔE_{ads} + D3 values decrease due to a decrease in the nanopore size but they are still higher than ΔE_{ads} + D3 values for the 10-crown-2…ion complexes.

As seen from Fig. 5, the presence of two, three and four O atoms in the nanopores increases the adsorption energy of Hg^{2+}, Cd^{2+}, and Pb^{2+} ions on the surfaces with respect to circumcircumcoronene surface, while the presence of six O atoms in the nanopores decreases the ΔE_{ads} + D3 of Hg^{2+} and Cd^{2+} ions on the 18-crown-6 surface with respect to circumcircumcoronene surface. This is due to increasing size of nanopore in the 18-crown-6 surface with respect to 10-crown-2, 12-crown-3 and 14-crown-4 surfaces [29].

The adsorption of Pb^{2+} ion on the 18-crown-6 surface is different from other surfaces. Our calculations indicate that the size of Pb^{2+} ion is similar to the nanopore size in 18-crown-6 surface. This leads to favorable interaction of the Pb^{2+} ion with the six O atoms on the surface and increases the ΔE_{ads} + D3 value with respect to other surfaces. Furthermore, the

Table 1 Thermochemistry calculations for adsorption of Hg^{2+}, Cd^{2+}, and Pb^{2+} ions on the surfaces, including adsorption energy (ΔE_{ads} in kcal/mol), adsorption energy corrected by Grimme's D3 correction (ΔE_{ads} + D3 in kcal/mol), enthalpy of adsorption (ΔH_{ads} in kcal/mol), and free energy of adsorption (ΔG_{ads} in kcal/mol)

Structure	ΔE_{ads} (ΔE_{ads} + D3)	ΔH_{ads}	ΔG_{ads}
Circumcircumcoronene…Hg^{2+}	− 308.4 (− 314.6)	− 308.8	− 304.9
Circumcircumcoronene…Cd^{2+}	− 242.8 (− 248.1)	− 242.8	− 239.7
Circumcircumcoronene…Pb^{2+}	− 130.2 (− 141.2)	− 133.3	− 124.2
10-crown-2…Hg^{2+}	− 327.1 (− 334.5)	− 328.3	− 323.5
10-crown-2…Cd^{2+}	− 261.4 (− 267.7)	− 262.29	− 257.7
10-crown-2…Pb^{2+}	− 151.3 (− 161.2)	− 154.9	− 146.4
12-crown-3…Hg^{2+}	− 371.9 (− 382.9)	− 373.4	− 367.7
12-crown-3…Cd^{2+}	− 306.5 (− 314.7)	− 308	− 300.4
12-crown-3…Pb^{2+}	− 169.8 (− 181.9)	− 173.9	− 166
14-crown-4…Hg^{2+}	− 356.5 (− 366.6)	− 358.6	− 352.4
14-crown-4…Cd^{2+}	− 291.1 (− 299.1)	− 292.44	− 287.7
14-crown-4…Pb^{2+}	− 149.3 (− 162.0)	− 161.6	− 155.4
18-crown-6…Hg^{2+}	− 301.5 (− 305.8)	− 304	− 303.3
18-crown-6…Cd^{2+}	− 235.7 (− 238.9)	− 238	− 235.1
18-crown-6…Pb^{2+}	− 179.5 (− 195.0)	− 186.7	− 178.1

Table 2 The nearest distance of ions from the surfaces (d in Å), charge on the ions in the surface…ion complexes (in e), and HOMO–LUMO energy gaps (E_g in kcal/mol) of the surface…ion complexes

Structure	d	Charge on the ions[a]	E_g[b]
Circumcircumcoronene…Hg^{2+}	4.054	0.0068	39.20
Circumcircumcoronene…Cd^{2+}	4.186	0.0406	39.20
Circumcircumcoronene…Pb^{2+}	2.256	0.5430	58.11
10-crown-2…Hg^{2+}	3.933	0.0392	43.58
10-crown-2…Cd^{2+}	4.000	0.0502	50.73
10-crown-2…Pb^{2+}	2.560	0.5999	65.49
12-crown-3…Hg^{2+}	3.817	0.0398	78.63
12-crown-3…Cd^{2+}	4.275	0.0437	74.25
12-crown-3…Pb^{2+}	2.358	0.6257	66.41
14-crown-4…Hg^{2+}	3.898	0.0357	74.48
14-crown-4…Cd^{2+}	4.172	0.0433	67.79
14-crown-4…Pb^{2+}	2.836	0.3413	46.81
18-crown-6…Hg^{2+}	3.667	0.0278	29.74
18-crown-6…Cd^{2+}	3.800	0.0762	32.05
18-crown-6…Pb^{2+}	2.740	0.8807	54.65

[a]Charge transfer (Q_{CT}) between the surfaces and ions is evaluated through calculating the charge difference of Hg^{2+}, Cd^{2+} and Pb^{2+} ions in isolated state and complexed with the surfaces

[b]$E_g = E_{(LUMO)} - E_{(HOMO)}$. The energy of HOMO and LUMO orbitals is found in Table S1 in the supporting information

performance of graphene-based materials in removal of metal ions from water samples has been studied using DFT calculations in the literature. For example, Thompho et al. [49] performed a systematic DFT study of the adsorption of Pb^{2+}, Cd^{2+}, Zn^{2+}, and Cu^{2+} on a GO surface. Their results reveal that the binding of Cu^{2+} to the GO surface is much stronger than that of other divalent metal ions. Kong et al. [13] also considered the adsorption mechanism of Na^{+}, Cu^{2+}, and Pb^{2+} metal ions at the GO surface. They found that the adsorption capacity of these metal ions on the GO surface follows the order $Pb^{2+} > Cu^{2+} > Na^{+}$. El-Fawal et al. [14] have used a DFT calculation to determine the removal mechanism of Zn^{2+}, Ni^{2+}, and Cr^{6+} hydrates by the prepared Fe_3O_4/GO hybrid. Their DFT results show that the coordination of Zn^{2+} hydrate with Fe_3O_4/GO is more favorable than the Ni^{2+} and Cr^{6+} hydrates and follows the order $Zn^{2+} > Ni^{2+} > Cr^{6+}$. It is worth mentioning that understanding the adsorption behavior of metal

ions on the surfaces is useful for design of effective control technologies for control of heavy metal pollution in industrial settings.

To explore the role of intermolecular interactions responsible for adsorption of metal ions on the surfaces, the noncovalent interaction (NCI) method presented by Yang et al. [50] was used. In this method, the attractive and repulsive interactions are recognized based on the electron density ($\rho(r)$) and the sign of the second derivative of electron density (λ_2) in the perpendicular direction of the bond. The noncovalent interaction index provides a 2D scatter plot of the reduced density gradient (RDG) versus the electron density. The RDG is defined by the following equation:

$$\mathrm{RDG} = \frac{|\nabla\rho(r)|}{2(3\pi^2)^{1/3}\rho(r)^{4/3}} \quad (2)$$

In order to distinguish the type of noncovalent interaction, the sign of λ_2 was utilized as a metric to identify bonded ($\lambda_2 < 0$) from non-bonded ($\lambda_2 > 0$) [50]. The gradient iso-surfaces are colored according to the corresponding values of sign(λ_2)ρ. Large negative values of sign(λ_2)ρ are indicative of attractive interactions (such as dipole–dipole, hydrogen bonding, halogen bonding and electrostatic); while large and positive values of sign(λ_2)ρ show repulsion interactions (such as steric effects in ring and cage). Finally, van der Waals (vdW) interactions are specified by a small value of λ_2 ($\lambda_2 \approx 0$) [50]. For the 3D color plot of the RDG iso-surfaces, a guide of the interpretations for various colors is provided: the deeper blue colors show stronger attractive interactions, which correspond to the smaller negative numbers of the horizontal ordinate in the 2D scatter plot, while the deeper red colors show stronger repulsive interactions tantamount to larger positive numbers on the ordinate axis. The green colors indicate the vdW interactions, whose values are close to zero regardless of the negative or positive horizontal axis direction. The colors between blue and green show gradually weaker attractive interactions, and the colors between green and red show gradually stronger repulsive interactions [51].

To explore the type of noncovalent interactions in the adsorption of Hg^{2+}, Cd^{2+}, and Pb^{2+} ions on the surfaces, we focus on the 3D plot of RDG and 2D scatter plot of RDG versus sign(λ_2)ρ of the surface…ion complexes (Figures S1–S3). As seen from Figure S1, the green color between the Hg^{2+} and Cd^{2+} ions and carbon atoms of the

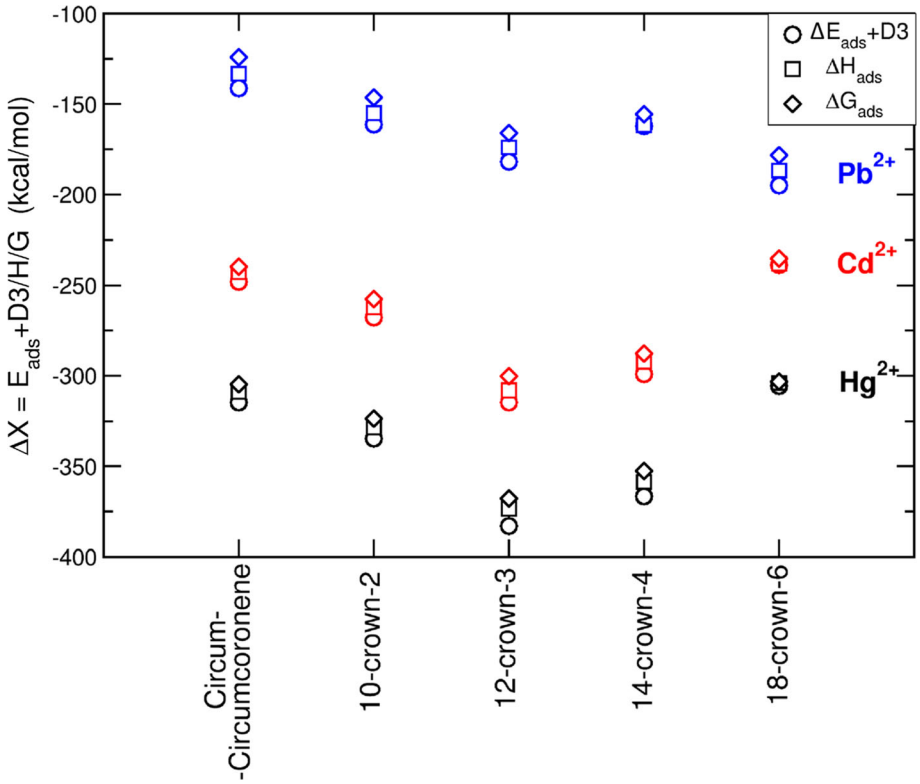

Figure 5 The change of adsorption energy (ΔE_{ads} + D3), enthalpy of adsorption (ΔH_{ads}) and free energy of adsorption (ΔG_{ads}) of the surface…ion (ion = Hg^{2+}, Cd^{2+}, and Pb^{2+}) complexes.

circumcircumcoronene surface shows the role of weak van der Waals interactions responsible for the adsorption of these ions on the circumcircumcoronene surface. These interactions can be seen in the 2D scatter plots where the numerical values are close to zero. From the RDG plot and the 2D scatter plot of the circumcircumcoronene…Pb^{2+} complex, it is observed that the electrostatic interactions are the only attractive interactions responsible for the adsorption of Pb^{2+} ion on the circumcircumcoronene surface. In the case of 10-crown-2…Hg^{2+} and 10-crown-2…Cd^{2+} complexes, the vdW interactions are observed between the C and O atoms of the 10-crown-2 surface and Hg^{2+} and Cd^{2+} ions. Small blue iso-surfaces in the RDG plots are related to the interactions between the oxygen atoms in the 10-crown-2 surface, which correspond to the scattered points in the 2D scatter plots of the 10-crown-2…Hg^{2+} and 10-crown-2…Cd^{2+} complexes. For the 10-crown-2…Pb^{2+} complex, the interaction between the Pb^{2+} ion and C atoms of the 10-crown-2 surface can be concluded to be electrostatic in nature, while O atom in the surface interacts with the Pb^{2+} ion through weak vdW interactions.

As one goes from the 10-crown-2 to 14-crown-4 surface, the interaction between the O atoms on the surface decreases. In the 12-crown-3/14-crown-4…Hg^{2+} and 12-crown-3/14-crown-4…Cd^{2+} complexes, the nature of interaction between the Hg^{2+} and Cd^{2+} ions turns out to be van der Waals in nature. Pb^{2+} ion interacts with the carbon atoms via electrostatic interactions while it interacts with the oxygen atoms through vdW interactions. However, the Pb^{2+} interaction is primarily vdW in nature when is adsorbed on the 14-crown-4 surface. As seen from Figure S3, the interaction of Hg^{2+} and Cd^{2+} ions with the O atoms on the 18-crown-6 surface is vdW in nature, while the O atoms through electrostatic interactions adsorb Pb^{2+} ion.

From our findings, it can be concluded that the Pb^{2+} ion is mainly adsorbed on the surfaces through electrostatic interactions, while Hg^{2+} and Cd^{2+} ions are adsorbed through vdW interactions. The reason for the difference in the nature of the interaction of Pb^{2+} ion with respect to Hg^{2+} and Cd^{2+} ions can be related to the difference in their electron configurations (Hg^{2+} ([Xe] $4f^{14}$ $5d^{10}$), Cd^{2+} ([Kr] $4d^{10}$), and Pb^{2+} ([Xe] $4f^{14}$ $5d^{10}$ $6s^2$)). According to the electron configurations, Pb^{2+} ion has vacant p orbitals and can interact with the π bonds in the circumcircumcoronene surface and oxygen atoms in the nanopores through electrostatic interactions. In comparison with Pb^{2+} ion, Hg^{2+} and Cd^{2+} ions do not have vacant orbitals. Thus, they have to interact with the surfaces only through vdW interactions. Furthermore, Hg^{2+} ion has a larger effective ionic radius (102 pm) than Cd^{2+} ion (95 pm) and thus it has more vdw interactions with the surfaces [52].

A key question from the findings is that why does Pb^{2+} ion with electrostatic interactions have a lower adsorption energy in comparison to Hg^{2+} and Cd^{2+} ions which generally interact with the surfaces via vdw forces, despite the chemical knowledge that electrostatic interactions are stronger in nature when compared to vdW interactions.

In order to answer this question, energy decomposition analysis (EDA) and Hirshfeld charge analysis were performed on the surface…ion complexes to understand the magnitude of charge transfer and its role in different adsorption strength of ions on the surfaces. The EDA was performed by using combined fragment wavefunctions, implemented in Multiwfn-3.7 program [41]. In this method, the total energy variation of forming a complex can be decomposed as:

$$\begin{aligned}\Delta E_{\text{tot}} &= E^{\text{Complex}} - \sum_i E_i^{\text{frag}} \\ &= (\Delta E_{\text{els}} + \Delta E_{\text{ex}}) + \Delta E_{\text{orb}} = \Delta E_{\text{steric}} + \Delta E_{\text{polar}}\end{aligned} \tag{3}$$

where ΔE_{els} is electrostatic interaction term; ΔE_{ex} is exchange repulsion term, which comes from the Pauli repulsion effect and is invariably positive. The exchange repulsion and electrostatics are normally combined to yield the steric term (ΔE_{steric}). ΔE_{orb} is orbital interaction term, often referred to induction or polarization term. ΔE_{orb} arises from the mixing of occupied molecular orbitals (MOs) and virtual MOs. The combined wavefunction is used as initial guess for the complex and ΔE_{orb} can be evaluated by subtracting the first self-consistent field (SCF) iteration energy from the last SCF iteration energy.

$$\Delta E_{\text{orb}} = E_{\text{SCF,last}} - E_{\text{SCF,1st}} \tag{4}$$

Note that $E_{\text{SCF,last}} = E^{\text{complex}}$, hence the following relationship:

$$\begin{aligned}\Delta E_{\text{steric}} &= \Delta E_{\text{els}} + \Delta E_{\text{ex}} = \Delta E_{\text{tot}} - \Delta E_{\text{orb}} \\ &= E_{\text{SCF,1st}} - \sum_i E_i^{\text{frag}}\end{aligned} \tag{5}$$

ΔE_{disp} (dispersion energy) component in total interaction energy is calculated by using the dispersion-corrected DFT methods. This term is the difference between the total energy obtained from DFT-D3 and DFT methods [53], CAM-B3LYP and CAM-B3LYP-D3 methods. Hence, by going from CAM-B3LYP to CAM-B3LYP-D3 methods, other terms, including ΔE_{orb} and $\Delta E_{els} + \Delta E_{ex}$ remain unchanged while the D3-dispersion correction is obtained as a new term.

Table 3 lists the results of EDA for the surface…ion complexes. On the other hand, the contribution of ΔE_{orb}, $\Delta E_{els} + \Delta E_{ex}$, and ΔE_{disp} components for the surface…ion complexes are shown in Fig. 6. As seen from Fig. 6, the contribution of the ΔE_{orb} component in the calculated interaction energies of the surface…ion complexes is greater than that of $\Delta E_{els} + \Delta E_{ex}$ and ΔE_{disp} components ($\Delta E_{orb} > \Delta E_{els} + \Delta E_{ex} > \Delta E_{disp}$). From the EDA results, it can be concluded that charge-transfer interactions are the primary energy contributors in the formation of surface…ion complexes. It is worth mentioning that the contribution of ΔE_{orb} component in the surface…Hg^{2+} complexes is more than that in the surface…Cd^{2+} and surface…Pb^{2+} complexes, following the order: surface…Hg^{2+} > surface…Cd^{2+} > surface…Pb^{2+}. This result is in agreement with the predicted adsorption energy order ΔE_{ads} + D3(surface…Hg^{2+}) > ΔE_{ads} + D3(surface…Cd^{2+}) > ΔE_{ads} + D3 (surface…Pb^{2+}). This also reveals that the surface…Hg^{2+} complexes have the highest adsorption energy due to having the highest contribution of charge transfer with respect to surface…Cd^{2+} and surface…Pb^{2+} complexes.

We also calculated the magnitude of charge transfer (Q_{CT}) between the ions and surfaces through computing the residual Hirshfeld charge on the ions in the surface…ion complexes (Table 2). Our charge analysis shows that the residual charge on the ions decreases upon interaction with the surfaces, indicating that the charge transfer process occurs from the surfaces to the ions. From Table 2, it is found that the magnitude of Q_{CT} in the surface…Hg^{2+} complexes is more that surface…Cd^{2+} and surface…Pb^{2+} complexes, following the order surface…Hg^{2+} > surface…Cd^{2+} > surface…Pb^{2+}. This result is in agreement with the observed trend for the ΔE_{orb} components and adsorption energy (ΔE_{ads} + D3) of these complexes.

From EDA, charge analysis and NCI plots, it is concluded that the charge transfer process from the surfaces to ions is a key mechanism for adsorption of these ions on the surfaces. On the other hand, the role of charge transfer in the formation of surface…ion complexes is more important than noncovalent interactions. Therefore, surface…Hg^{2+} and surface…Cd^{2+} complexes, despite having weaker noncovalent interactions, have more ΔE_{ads} + D3 values than surface…Pb^{2+} complexes due to their higher charge transfer values.

Furthermore, Fig. 7 shows that there is a good correlation between the ΔE_{orb} obtained from EDA and HOMO–LUMO energy gap (E_g) of the surface…ion complexes, summarized in Table 2. According to this correlation, an increase in the contribution of ΔE_{orb} in the surface…ion complexes leads to an increase in the E_g values of the complexes and their stability. The greater the band-gap, the larger is the effects of polarization.

The UV–visible absorption spectra of different sizes of graphene nanoflakes have been simulated using TD-DFT calculations by Silva et al. [54]. Their results indicate that different sizes of graphene nanoflakes produce a visible region, which is a suitable criterion to produce light-emitting devices. We have also investigated the effect of Hg, Cd and Pb atoms adsorption on the electronic and optical properties of graphene, sulfur and nitrogen/sulfur co-doped graphene surfaces and nitrogen-coordinated defective graphene quantum dots in our previous studies [47, 48]. Our results indicate that the strong bands in the absorption spectra of the surfaces are shifted and new bands appear with adsorption of Hg, Cd, and Pb metal atoms. In this context, the similar technique was used to highlight the effect of Hg^{2+}, Cd^{2+}, and Pb^{2+} ions adsorption on the optical properties of circumcircumcoronene and GNFs containing oxygen-passivated nanopores. The UV–visible spectra of these surfaces and their complexes with the ions are shown in Fig. 8. The data related to the absorption bands are summarized in Table S2.

As seen from Fig. 8, circumcircumcoronene surface shows a strong band at λ = 449.62 nm (HOMO-1 → LUMO + 1), which corresponds to the $\pi \rightarrow \pi^*$ electronic transitions due to the presence of C=C bonds. Our results reveal that the creation of oxygen-passivated nanopores in the GNF surface changes the shape and position of the absorption peak observed in the circumcircumcoronene spectrum. It is observed that the peak at λ = 449.62 nm is red-shifted, except in the case of 18-crown-6 surface. Furthermore, new

Table 3 The energy decomposition analysis (EDA (kcal/mol)) of the surface…ion complexes calculated at the CAM-B3LYP(CAM-B3LYP-D3)/6–31g(*d*,*p*)/Def2-TZVPP level of theory

Structure	ΔE_{orb}	$\Delta E_{els} + \Delta E_{ex}$	ΔE_{disp}	ΔE_{tot}	ΔE_{tot} + D3
Circumcircumcoronene…Hg^{2+}	− 350.93	− 14.1	− 6.27	− 365.03	− 371.30
Circumcircumcoronene…Cd^{2+}	− 285.45	− 13.69	− 5.41	− 299.14	− 304.55
Circumcircumcoronene…Pb^{2+}	− 232.76	43.39	− 11.05	− 189.37	− 200.42
10-crown-2…Hg^{2+}	− 373.24	− 14.74	− 7.41	− 387.98	− 395.39
10-crown-2…Cd^{2+}	− 307.63	− 14.47	− 6.30	− 322.10	− 328.40
10-crown-2…Pb^{2+}	− 255.34	35.39	− 9.88	− 219.95	− 229.83
12-crown-3…Hg^{2+}	− 422.64	− 11.68	− 10.06	− 434.32	− 444.38
12-crown-3…Cd^{2+}	− 356.99	− 10.56	− 8.18	− 367.55	− 375.73
12-crown-3…Pb^{2+}	− 265.27	15.87	− 12.13	− 249.40	− 261.53
14-crown-4…Hg^{2+}	− 400.30	− 17.65	− 10.06	− 417.95	− 428.01
14-crown-4…Cd^{2+}	− 336.15	− 15.66	− 7.97	− 351.81	− 359.78
14-crown-4…Pb^{2+}	− 182.58	− 27.21	− 12.79	− 209.79	− 222.58
18-crown-6…Hg^{2+}	− 318.86	− 36.59	− 9.79	− 355.46	− 365.25
18-crown-6…Cd^{2+}	− 252.37	− 36.55	− 8.49	− 288.92	− 297.41
18-crown-6…Pb^{2+}	− 173.43	− 68.08	− 15.49	− 241.51	− 257.00

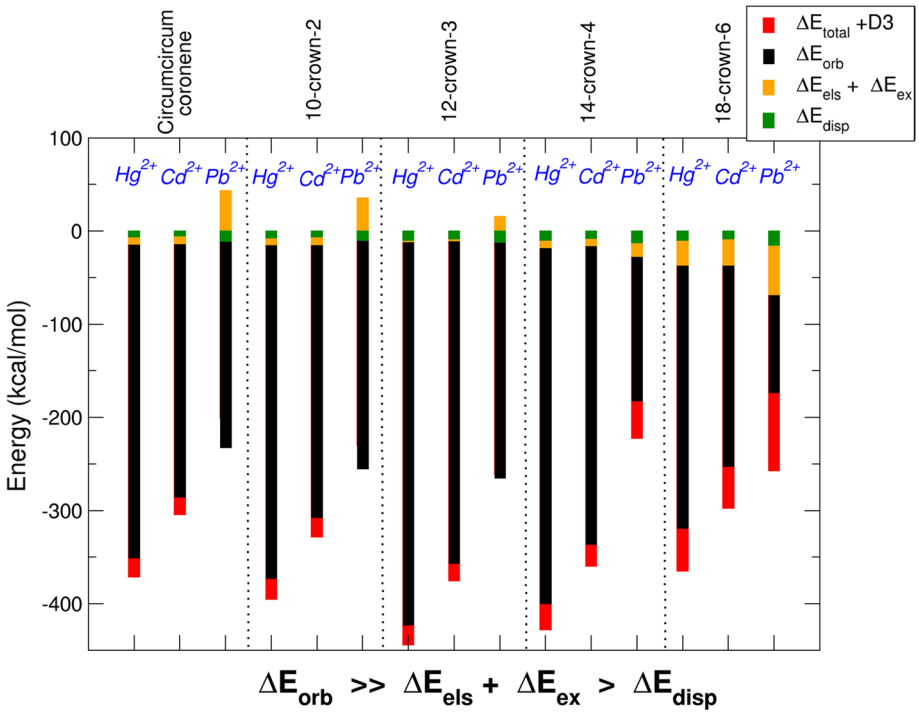

Figure 6 The contribution of ΔE_{orb}, $\Delta E_{els} + \Delta E_{ex}$, and ΔE_{disp} components in the total energy variation of forming surface…ion complexes (ΔE_{tot} + D3) calculated at the CAM-B3LYP(CAM-B3LYP-D3)/6–31g(*d*,*p*)/Def2-TZVPP level of theory.

peaks appear, which can be related to the appearance of new electronic transitions of n(O) → π*(C=C).

Upon adsorption of Hg^{2+} ion on the circumcircumcoronene surface, the main peak at λ = 449.62 nm is red-shifted to λ = 497.46 nm, while a large quenching occurs for this peak with adsorption of Cd^{2+} and Pb^{2+} ions. On the other hand, a new peak appears at λ = 605.28 nm with adsorption of Hg^{2+} ion as well as at λ = 605.31 nm with adsorption of Cd^{2+} ion in the absorption spectrum of circumcircumcoronene surface. It is worth mentioning that several new peaks in the near-infrared region appear in the range of 900–1150 nm. These new peaks are related to the electronic transitions from HOMO-1, HOMO-2 and HOMO-3 orbitals to LUMO and LUMO + 1 orbitals.

There are two strong absorption bands in the 10-crown-2 spectrum. The first absorption band at

λ = 434.74 nm (HOMO-2 → LUMO) has a higher intensity and oscillator strength than the second band at λ = 526.38 nm (HOMO-1 → LUMO). These absorption bands are red-shifted and their intensity change with adsorption of Hg^{2+}, Cd^{2+}, and Pb^{2+} ions. In the 12-crown-3 spectrum, two absorption bands are observed at λ = 650.63 nm and λ = 918.97 nm, which are related to the HOMO-2 → LUMO and HOMO → LUMO + 2 electronic transitions, respectively. These absorption bands are red-shifted with adsorption of Hg^{2+}, Cd^{2+}, and Pb^{2+} ions.

According to the Fig. 8, the pattern of UV–visible spectra of 12-crown-3…Hg^{2+} and 12-crown-3…Cd^{2+} complexes are similar and the highest changes are seen in the 12-crown-3…Pb^{2+} spectrum. One strong absorption band along with two weak absorption bands are observed in the 14-crown-4 spectrum. The λ = 501.31 nm (HOMO-1 → LUMO) is associated with the strong absorption band. This band is red-shifted with adsorption of Hg^{2+}, Cd^{2+}, and Pb^{2+} ions. It should be mentioned that the effect of Hg^{2+} and Cd^{2+} ions on the absorption spectrum of 14-crown-4 surface is similar. The point to note is that the adsorption of Hg^{2+}, Cd^{2+} and Pb^{2+} ions on the 10-crown-2, 12-crown-3, and 14-crown-4 surfaces lead to the appearance of weak peaks in the absorption spectrum of the surfaces.

In the 18-crown-6 spectrum, only a broad absorption band is seen at λ = 403.05 nm, which is associated to the HOMO-2 → LUMO + 1 transition. A similar effect of red-shifting on the 18-crown-6 spectrum was observed with interaction of Hg^{2+} and Cd^{2+} ions. These interactions also lead to appearance of a new broad band in the near-infrared region of the 18-crown-6…Hg^{2+} and 18-crown-6…Cd^{2+} spectra at λ = 1615.08 nm (HOMO-4 → LUMO) and λ = 1617.70 nm (HOMO-4 → LUMO), respectively. With interaction of Pb^{2+} ion, the absorption band at λ = 403.05 nm is quenched and a new broad band appears at λ = 1517.16 nm, which is associated with the HOMO-2 → LUMO transition. The red-shifting of the peaks upon adsorption of ions on such surfaces could be used for detection of toxic heavy elements from contaminated environments. On the other hand, the presence of near-infra-red peaks could find potential applications in design of near-infrared photonic devices [55], ultrafast nonlinear photonic devices [56], laser line optics for specific wavelengths [57], infrared imaging and vision applications [58], new near-IR spectroscopic sensing systems that need to be portable and cost-effective [59], and near-infrared light-responsive shape memory photonic crystals (SMPCs) [60].

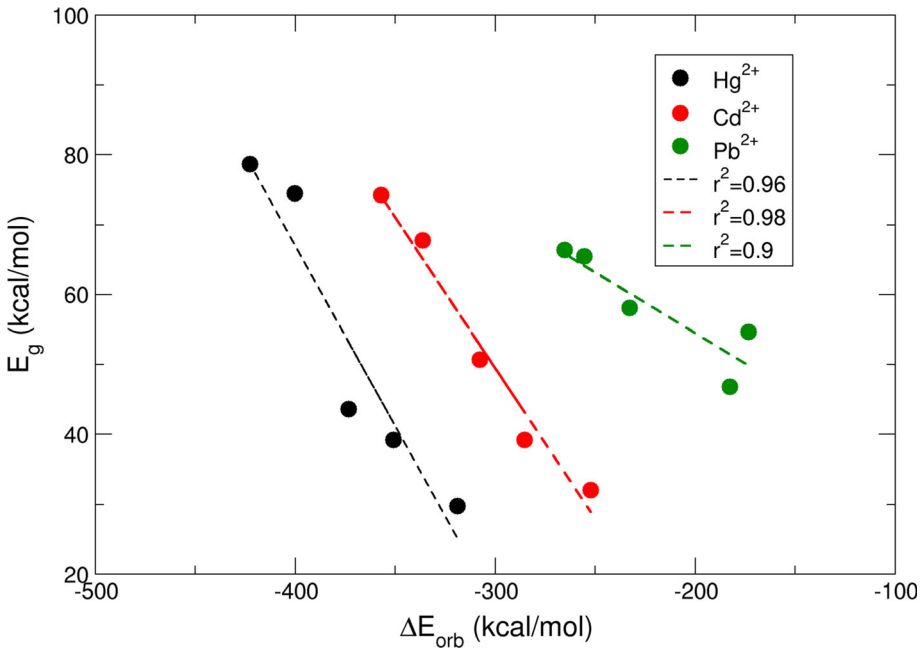

Figure 7 Correlation between the ΔE_{orb} obtained from EDA and HOMO–LUMO energy gap (E_g) of the surface…ion complexes.

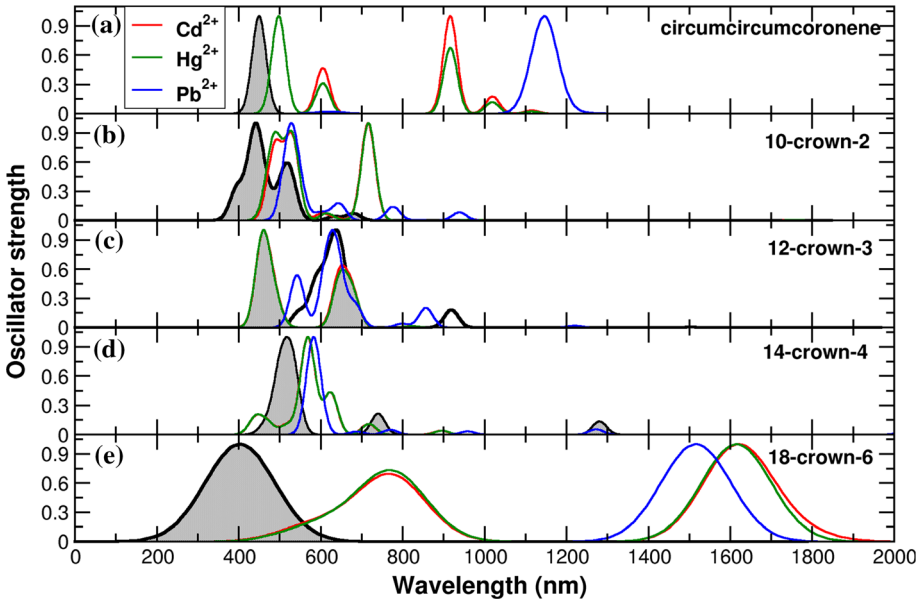

Figure 8 Changes in the UV–visible absorption spectra of the surfaces with adsorption of Hg^{2+}, Cd^{2+}, and Pb^{2+} ions, calculated at the CAM-B3LYP/6–31g(*d*,*p*)/Def2-TZVPP level of theory.

Conclusions

In summary, we have investigated the interactions of Hg^{2+}, Cd^{2+}, and Pb^{2+} ions with pristine graphene nanoflake (GNF) model (circumcircumcoronene) and the GNFs containing oxygen-passivated nanopores (10-crown-2, 12-crown-3, 14-crown-4, and 18-crown-6) using CAM-B3LYP(CAM-B3LYP-D3)/6–31g(*d*,*p*)/Def2-TZVPP method. Electrostatic potential (ESP) isosurface shows that the oxygen atoms in the nanopores have the highest negative electrostatic potential and reactivity for interaction with ions. Our DFT results show that Hg^{2+} ion has the maximum adsorption energy (ΔE_{ads}) on all of the surfaces and the sequence of the adsorption strength is $Hg^{2+} > Cd^{2+} > Pb^{2+}$. Furthermore, it is found that the number of oxygen atoms in the nanopores and the size of nanopores affect the adsorption strength of ions. These two effects lead to the order 12-crown-3 > 14-crown-4 > 10-crown-2 > circumcircumcoronene > 18-crown-6 for adsorption of Hg^{2+} and Cd^{2+} ions as well as the order 18-crown-6 > 12-crown-3 > 14-crown-4 > 10-crown-2 > circumcircumcoronene for adsorption of Pb^{2+} ion.

The EDA results indicate that the ions are adsorbed on the surfaces through charge transfer from the surfaces to the ions. Hirshfeld charge analysis reveals that the magnitude of charge transfer in the surface…Hg^{2+} complexes is more than that in the surface…Cd^{2+} and surface…Pb^{2+} complexes and follows the order surface…Hg^{2+} > surface…Cd^{2+} > surface…Pb^{2+}. The NCI plots indicate that the important noncovalent interaction for adsorption of Pb^{2+} ion on the surfaces is electrostatic interaction, while it is vdW interaction for adsorption of Hg^{2+} and Cd^{2+} ions. The UV–visible absorption spectra of the oxygen-passivated nanopores are mostly related to the π(C=C) → π^*(C=C) and n(O) → π^*(C=C) transitions. Our TD-DFT calculations indicate that the adsorption of ions on the surfaces leads to significant changes on their absorption spectra, including peak shifts, peak quenching and appearance of new peaks. The results of this study in understanding the adsorption mechanism of toxic heavy metal ions on the nanopores are useful for design of effective control technologies for control of toxic heavy ion pollution in contaminated environments and industrial settings.

Supporting information

This material contains the energy of HOMO and LUMO orbitals, NCI plots, and the TD-DFT results of the surface…ion complexes.

Acknowledgements

We gratefully acknowledge financial support from the Research Council of Jahrom University and Birjand University of Technology.

Electronic supplementary material: The online version of this article (https://doi.org/10.1007/s10853-020-05113-4) contains supplementary material, which is available to authorized users.

References

[1] Jaishankar M, Tseten T, Anbalagan N, Mathew BB, Beeregowda KN (2014) Toxicity, mechanism and health effects of some heavy metals. Interdiscip Toxicol 7(2):60–72. https://doi.org/10.2478/intox-2014-0009

[2] Singh R, Gautam N, Mishra A, Gupta R (2011) Heavy metals and living systems: an overview. Indian J Pharmacol 43(3):246–253. https://doi.org/10.4103/0253-7613.81505

[3] https://www.who.int/ipcs/assessment/public_health/chemicals_phc/en/

[4] Novoselov KS, Jiang D, Schedin F, Booth T, Khotkevich V, Morozov S, Geim AK (2005) Two-dimensional atomic crystals. Proc Natl Acad Sci 102(30):10451–10453. https://doi.org/10.1073/pnas.0502848102

[5] Xu J, Cao Z, Zhang Y, Yuan Z, Lou Z, Xu X, Wang X (2018) A review of functionalized carbon nanotubes and graphene for heavy metal adsorption from water: preparation, application, and mechanism. Chemosphere 195:351–364. https://doi.org/10.1016/j.chemosphere.2017.12.061

[6] Sherlala AIA, Raman AAA, Bello MM, Asghar A (2018) A review of the applications of organo-functionalized magnetic graphene oxide nanocomposites for heavy metal adsorption. Chemosphere 193:1004–1017. https://doi.org/10.1016/j.chemosphere.2017.11.093

[7] Peng W, Li H, Liu Y, Song S (2017) A review on heavy metal ions adsorption from water by graphene oxide and its composites. J Mol Liq 230:496–504. https://doi.org/10.1016/j.molliq.2017.01.064

[8] Yang Z-y, Dai N-n, Lu R-t, Huang Z-h, Kang F-y (2016) A review of graphene composite-based sensors for detection of heavy metals. Carbon 100(104):260–262. https://doi.org/10.1016/j.carbon.2015.12.055

[9] Chang J, Zhou G, Christensen ER, Heideman R, Chen J (2014) Graphene-based sensors for detection of heavy metals in water: a review. Anal Bioanal Chem 406(16):3957–3975. https://doi.org/10.1007/s00216-014-7804-x

[10] Abu-Nada A, McKay G, Abdala A (2020) Recent advances in applications of hybrid graphene materials for metals removal from wastewater. Nanomaterials 10(3):595–627. https://doi.org/10.3390/nano10030595

[11] Kommu A, Singh JK (2020) A review on graphene-based materials for removal of toxic pollutants from wastewater. Soft Mater. https://doi.org/10.1080/1539445X.2020.1739710

[12] Guerrero-Fajardo CA, Giraldo L, Moreno-Piraján JC (2020) Preparation and characterization of graphene oxide for Pb(II) and Zn(II) ions adsorption from aqueous solution: experimental, thermodynamic and kinetic study. Nanomaterials 10(6):1022–1050. https://doi.org/10.3390/nano10061022

[13] Kong Q, Preis S, Li L, Luo P, Wei C, Li Z, Hu Y, Wei C (2020) Relations between metal ion characteristics and adsorption performance of graphene oxide: a comprehensive experimental and theoretical study. Sep Purif Technol 232:115956. https://doi.org/10.1016/j.seppur.2019.115956

[14] El-Fawal EM, Saad L, Moustafa YM (2020) Computational DFT study of magnetite/graphene oxide nanoadsorbent: interfacial chemical behavior and remediation performance of heavy metal hydrates from aqueous system. Water Environ Res. https://doi.org/10.1002/wer.1325

[15] Berber MR (2020) Current advances of polymer composites for water treatment and desalination. J Chem 2020:1–18. https://doi.org/10.1155/2020/7608423

[16] Li L, Zhao L, Ma J, Tian Y (2020) Preparation of graphene oxide/chitosan complex and its adsorption properties for heavy metal ions. Green Process Synth 9(1):294–303. https://doi.org/10.1515/gps-2020-0030

[17] Lee J, Yang Z, Zhou W, Pennycook SJ, Pantelides ST, Chisholm MF (2014) Stabilization of graphene nanopore. Proc Natl Acad Sci 111(21):7522–7526. https://doi.org/10.1073/pnas.1400767111

[18] Xiao J, Mei D, Li X, Xu W, Wang D, Graff GL, Bennett WD, Nie Z, Saraf LV, Aksay IA, Liu J, Zhang J-G (2011) Hierarchically porous graphene as a lithium-air battery electrode. Nano Lett 11(11):5071–5078. https://doi.org/10.1021/nl203332e

[19] Datta D, Li J, Shenoy VB (2014) Defective graphene as a high-capacity anode material for Na- and Ca-ion batteries. ACS Appl Mater Interfaces 6(3):1788–1795. https://doi.org/10.1021/am404788e

[20] O'Hern SC, Boutilier MSH, Idrobo J-C, Song Y, Kong J, Laoui T, Atieh M, Karnik R (2014) Selective ionic transport through tunable subnanometer pores in single-layer graphene membranes. Nano Lett 14(3):1234–1241. https://doi.org/10.1021/nl404118f

[21] Rollings RC, Kuan AT, Golovchenko JA (2016) Ion selectivity of graphene nanopores. Nat Commun 7:11408–11414. https://doi.org/10.1038/ncomms11408

[22] Surwade SP, Smirnov SN, Vlassiouk IV, Unocic RR, Veith GM, Dai S, Mahurin SM (2015) Water desalination using nanoporous single-layer graphene. Nat Nanotechnol 10(5):459–464. https://doi.org/10.1038/nnano.2015.37

[23] Bell DC, Lemme MC, Stern LA, Williams JR, Marcus CM (2009) Precision cutting and patterning of graphene with helium ions. Nanotechnology 20(45):455301–455307. https://doi.org/10.1088/0957-4484/20/45/455301

[24] Bieri M, Treier M, Cai J, Aït-Mansour K, Ruffieux P, Gröning O, Gröning P, Kastler M, Rieger R, Feng X, Müllen K, Fasel R (2009) Porous graphenes: two-dimensional polymer synthesis with atomic precision. ChemComm 45:6919–6921. https://doi.org/10.1039/b915190g

[25] Kim M, Safron NS, Han E, Arnold MS, Gopalan P (2010) Fabrication and characterization of large-area, semiconducting nanoperforated graphene materials. Nano Lett 10(4):1125–1131. https://doi.org/10.1021/nl9032318

[26] Russo CJ, Golovchenko JA (2012) Atom-by-atom nucleation and growth of graphene nanopores. Proc Natl Acad Sci 109(16):5953–5957

[27] Tsetseris L, Pantelides ST (2009) Adatom complexes and self-healing mechanisms on graphene and single-wall carbon nanotubes. Carbon 47(3):901–908. https://doi.org/10.1016/j.carbon.2008.12.002

[28] Zan R, Ramasse QM, Bangert U, Novoselov KS (2012) Graphene reknits its holes. Nano Lett 12(8):3936–3940. https://doi.org/10.1021/nl300985q

[29] Guo J, Lee J, Contescu CI, Gallego NC, Pantelides ST, Pennycook SJ, Moyer BA, Chisholm MF (2014) Crown ethers in graphene. Nat Commun 5(1):1–6. https://doi.org/10.1038/ncomms6389

[30] Maarouf AA, Nistor RA, Afzali-Ardakani A, Kuroda MA, Newns DM, Martyna GJ (2013) Crown graphene nanomeshes: highly stable chelation-doped semiconducting materials. J Chem Theory Comput 9(5):2398–2403. https://doi.org/10.1021/ct4000636

[31] Heath JJ, Kuroda MA (2018) First principles studies of the interactions between alkali metal elements and oxygen-passivated nanopores in graphene. Phys Chem Chem Phys 20(40):25822–25828. https://doi.org/10.1039/C8CP04958K

[32] Olsson E, Chai G, Dove M, Cai Q (2019) Adsorption and migration of alkali metals (Li, Na, and K) on pristine and defective graphene surfaces. Nanoscale 11(12):5274–5284. https://doi.org/10.1039/C8NR10383F

[33] Azamat J (2016) Functionalized graphene nanosheet as a membrane for water desalination using applied electric fields: insights from molecular dynamics simulations. J Phys Chem C 120(41):23883–23891. https://doi.org/10.1021/acs.jpcc.6b08481

[34] Cohen-Tanugi D, Grossman JC (2012) Water desalination across nanoporous graphene. Nano Lett 12(7):3602–3608. https://doi.org/10.1021/nl3012853

[35] Sint K, Wang B, Král P (2008) Selective ion passage through functionalized graphene nanopores. J Am Chem Soc 130(49):16448–16449. https://doi.org/10.1021/ja804409f

[36] Yanai T, Tew DP, Handy NC (2004) A new hybrid exchange–correlation functional using the Coulomb-attenuating method (CAM-B3LYP). Chem Phys Lett 393(1):51–57. https://doi.org/10.1016/j.cplett.2004.06.011

[37] Frisch M, Trucks G, Schlegel H et al (2009) Gaussian 09, Revision D. 01. Gaussian, Wallingford

[38] Boys SF, Bernardi F (1970) The calculation of small molecular interactions by the differences of separate total energies. Some procedures with reduced errors. Mol Phys 19(4):553–566. https://doi.org/10.1080/00268977000101561

[39] Grimme S, Antony J, Ehrlich S, Krieg H (2010) A consistent and accurate ab initio parametrization of density functional dispersion correction (DFT-D) for the 94 elements H-Pu. J Chem Phys 132(15):154104–154123. https://doi.org/10.1063/1.3382344

[40] Hirshfeld FL (1977) Bonded-atom fragments for describing molecular charge densities. Theor Chim Acta 44(2):129–138. https://doi.org/10.1007/BF00549096

[41] Lu T, Chen F (2012) Multiwfn: a multifunctional wavefunction analyzer. J Comput Chem 33:580–592. https://doi.org/10.1002/jcc.22885

[42] Humphrey W, Dalke A, Schulten K (1996) VMD: visual molecular dynamics. J Mol Graph 14(1):33–38. https://doi.org/10.1016/0263-7855(96)00018-5

[43] Runge E, Gross EKU (1984) Density-functional theory for time-dependent systems. Phys Rev Lett 52(12):997–1000. https://doi.org/10.1103/PhysRevLett.52.997

[44] Raghi KR, Sherin DR, Saumya MJ, Arun PS, Sobha VN, Manojkumar TK (2018) Computational study of molecular electrostatic potential, docking and dynamics simulations of gallic acid derivatives as ABL inhibitors. Comput Biol Chem 74:239–246. https://doi.org/10.1016/j.compbiolchem.2018.04.001

[45] Shtepliuk I, Yakimova R (2018) Interband transitions in closed-shell vacancy containing graphene quantum dots complexed with heavy metals. Phys Chem Chem Phys 20(33):21528–21543. https://doi.org/10.1039/C8CP03306D

[46] Shtepliuk I, Caffrey NM, Iakimov T, Khranovskyy V, Abrikosov IA, Yakimova R (2017) On the interaction of toxic heavy metals (Cd, Hg, Pb) with graphene quantum dots and infinite graphene. Sci Rep 7(1):1–17. https://doi.org/10.1038/s41598-017-04339-8

[47] Ghenaatian HR, Shakourian-Fard M, Kamath G (2019) The effect of sulfur and nitrogen/sulfur co-doping in graphene surface on the adsorption of toxic heavy metals (Cd, Hg, Pb).

J Mater Sci 54(20):13175–13189. https://doi.org/10.1007/s10853-019-03791-3

[48] Ghenaatian HR, Shakourian-Fard M, Moghadam MR, Kamath G, Rahmanian M (2019) Tailoring of graphene quantum dots for toxic heavy metals detection. Appl Phys A 125(11):754–765. https://doi.org/10.1007/s00339-019-3042-6

[49] Thompho S, Rungrotmongkol T, Saengsawang O, Hannongbua S (2017) A computational study of adsorption of divalent metal ions on graphene oxide. Songklanakarin J Sci Technol 39(6):773–778. https://doi.org/10.14456/sjst-psu.2017.94

[50] Johnson ER, Keinan S, Mori-Sánchez P, Contreras-García J, Cohen AJ, Yang W (2010) Revealing noncovalent interactions. J Am Chem Soc 132(18):6498–6506. https://doi.org/10.1021/ja100936w

[51] Cao S, Wang J, Ding Y, Sun M, Ma F (2017) Visualization of weak interactions between quantum dot and graphene in hybrid materials. Sci Rep 7(1):417–424. https://doi.org/10.1038/s41598-017-00542-9

[52] Marcus Y (1991) Thermodynamics of solvation of ions. Part 5.—Gibbs free energy of hydration at 298.15 K. J Chem Soc Faraday Trans 87(18):2995–2999. https://doi.org/10.1039/FT9918702995

[53] Fonseca Guerra C, Wijst T, Poater J, Swart M, Bickelhaupt FM (2010) Adenine versus guanine quartets in aqueous solution: dispersion-corrected DFT study on the differences in π-stacking and hydrogen-bonding behavior. Theor Chem Acc 125:245–252. https://doi.org/10.1007/s00214-009-0634-9

[54] Silva AM, Pires MS, Freire VN, Albuquerque EL, Azevedo DL, Caetano EWS (2010) Graphene nanoflakes: thermal stability, infrared signatures, and potential applications in the field of spintronics and optical nanodevices. J Phys Chem C 114(41):17472–17485. https://doi.org/10.1021/jp105728p

[55] Dahal R, Lin JY, Jiang HX, Zavada JM (2011) Near infrared photonic devices based on Er-doped GaN and InGaN. Opt Mater 33(7):1066–1070. https://doi.org/10.1016/j.optmat.2010.10.002

[56] Wang Z, Li H, Luo M, Chen T, Xia X, Chen H, Ma C, Guo J, He Z, Song Y, Liu J, Jiang X, Zhang H (2020) MXene photonic devices for near-infrared to mid-infrared ultrashort pulse generation. ACS Appl Nano Mater 3(4):3513–3522. https://doi.org/10.1021/acsanm.0c00241

[57] Zhang Y, Ye J, Xu J, Song J, Yao T, Zhou P (2020) Dual-wavelength random distributed feedback fiber laser with wavelength, linewidth, and power ratio tunability. Opt Express 28(7):10515–10523. https://doi.org/10.1364/OE.390796

[58] Türker-Kaya S, Huck CW (2017) A review of mid-infrared and near-infrared imaging: principles, concepts and applications in plant tissue analysis. Molecules 22(1):168–187. https://doi.org/10.3390/molecules22010168

[59] Marris-Morini D, Vakarin V, Ramirez JM, Liu Q, Ballabio A, Frigerio J, Montesinos M, Alonso-Ramos C, Roux XL, Serna S, Benedikovic D, Chrastina D, Vivien L, Isella G (2018) Germanium-based integrated photonics from near- to mid-infrared applications. Nanophotonics 7(11):1781–1793. https://doi.org/10.1515/nanoph-2018-0113

[60] Chang P, Niu W, Qu L, Zhang S (2019) Two-way rewritable and stable photonic patterns enabled by near-infrared laser-responsive shape memory photonic crystals. J Mater Chem C 7:1896–1903. https://doi.org/10.1039/D0TC00863J